Aerothermal Study of Mars Pathfinder Aeroshell

Roop N. Gupta*
NASA Langley Research Center, Hampton, Virginia 23681
K. P. Lee[†]
ViGYAN, Inc., Hampton, Virginia 23666
and
Carl D. Scott[‡]
NASA Johnson Space Center, Houston, Texas 77058

An aerothermodynamic study of the Mars Pathfinder aeroshell is carried out through a viscous-shock layer (VSL) analysis with and without surface ablation. Stagnation-point results are obtained along a specified trajectory, and detailed calculations along the body are provided at the peak-heating point. The formulation of VSL equations with a new length scale and the implementation of the Vigneron pressure condition predict the extent of the subsonic region and the surface pressure, which compare well with Navier–Stokes calculations. For equilibrium as well as nonequilibrium flow results, a gas composed of 16 species is used to model the shock layer for the Martian atmosphere (97% CO_2 and 3% N_2). A physically consistent surface recombination model (which allows for the diffusion limitation of reactants) for CO_2 is obtained. A parametric study at the trajectory peak-heating point suggests that surface catalysis has the largest effect on heating prediction. The maximum stagnation-point heating of 127 W/cm^2 is obtained at an altitude of 40.7 km from nonequilibrium chemistry calculations with fully recombined CO_2 as the surface boundary condition. Equilibrium chemistry gives a similar value for the nonablation case at this altitude. Calculations have also been carried out to evaluate the reduction in heating because of ablation. A decrease of about 9% in the stagnation-heating value (with equilibrium chemistry) is obtained at the peak-heating point.

Nomenclature

C_i = mass fraction of species i

$\bar{C}_k$ = mass fraction of element k, $\sum_i \delta_{ik}(M_k^*/M_i^*)C_i$

C_p = frozen specific heat of mixture, $\sum_i C_i C_{p,i}$

$C_{p,i}$ = specific heat of species i, $C_{p,i}^*/C_{p,\infty}^*$

$C_{1,r}, C_{2,r}, C_{3,r},$ = curve-fit coefficients for equilibrium
$C_{4,r}, C_{5,r}$ constants $K_{EQ,r}$

D_{i-j}^* = binary diffusion coefficient, m^2/s

D_m^* = effective diffusion coefficient for mixture, m^2/s

h_i = enthalpy of species i, h_i^*/U_∞^{*2}

J_i^* = mass flux of species i, kg/m^2 · s

K = thermal conductivity of mixture, $K^*/\mu^*(T_{ref}^*)C_{p,\infty}^*$

$K_{EQ,r}$ = equilibrium constant for reaction r, $k_{f,r}^*/k_{b,r}^*$

$k_{ads,i}^*$ = adsorption rate coefficient, m/s

$k_{b,r}^*$ = backward reaction rate coefficient for reaction r, cm/mole · s or cm^6/mole^2 · s

$k_{f,r}^*$ = forward reaction rate coefficient for reaction r, cm^3/mole · s

k_i^* = recombination rate coefficient, m/s

Le = Lewis number, $\rho^* D_{i-j}^* C_p^*/K^*$

M_∞ = freestream Mach number

M_i^* = molecular weight of species i

$\dot{m}$ = mass injection rate, $\dot{m}^*/\rho_\infty^* U_\infty^*$

N_i = number flux of species i, particles/m^2 · s

n = coordinate measured normal to body, n^*/R_{sh}^*

p_∞ = freestream pressure

q_{rad} = radiative heat transfer rate, $q_{rad}^*/(\rho_\infty^* U_\infty^{*3})$

q_w = wall heat transfer rate, $q_w^*/(\rho_\infty^* U_\infty^{*3})$

R_N^* = nose radius, m

R_{sh}^* = shoulder radius, m

R_{univ}^* = universal gas constant, 8314.3 J/kg- mole · K

r^* = radius measured from axis of symmetry to a point on the body surface

s^* = coordinate measured along the surface, m

T^* = temperature, K

$T_{D_{f,r}}^*$ = activation temperature for the forward reaction r, K

T_{REWT}^* = radiative equilibrium wall temperature, K

T_{ref}^* = reference temperature $U_\infty^{*2}/C_{p,\infty}^*$, K

U_∞^* = freestream velocity, m/s

v = velocity normal to body surface

x_i = mole fraction of species i

x^* = distance along the body axis, m

γ_i = recombination probability of species i

$\bar{\gamma}_i$ = adsorption probability of species i

δ_{ik} = number of atoms of the kth element in species i

$\bar{\varepsilon}$ = char emissivity, 0.78

$\bar{\varepsilon}_N$ = Reynolds-number parameter based on R_N^*, $(\mu_{ref}^*/\rho_\infty^* R_N^* U_\infty^*)^{1/2}$

$\bar{\varepsilon}_{sh}$ = Reynolds-number parameter based on R_{sh}^*, $(\mu_{ref}^*/\rho_\infty^* R_{sh}^* U_\infty^*)^{1/2}$

$\bar{\eta}$ = transformed normal coordinate, n/n_{sh}

μ = viscosity of mixture, μ^*/μ_{ref}^*

μ_{ref}^* = reference viscosity, $\mu^*(T_{ref}^*)$, N · s/m^2

ρ^* = density of mixture, kg/m^3

σ^* = Stefan–Boltzmann constant, 5.668×10^{-8} J/s · m^{2}K^4

Subscripts

E = entry

EQ = equilibrium

i	= ith species
j	= jth species
k	= kth element
w	= wall value
—	= gas–solid interface value resulting from surface ablation

Superscripts

des	= desorption
net	= net
↓	= incident
*	= dimensional quantity

Introduction

A VISCOUS shock layer (VSL) analysis of high-energy entry and aerobraking into the Martian atmosphere for a manned mission was reported in Ref. 1. Since that study, the Mars Environmental Survey (MESUR) concept[2] has been developed as a relatively low-cost, near-term approach to a Mars network mission which would be part of an evolutionary strategy for Mars exploration. This concept is to serve as a precursor to a series of robotic and human missions. Recently, the MESUR Pathfinder program has been suggested as a single-flight discovery program to obtain engineering information about launch, cruise, entry, descent, landing, rover, instruments, and scientific knowledge of the Martian atmosphere and surface.

Because of the large aerobrakes required for a manned missions, the analysis of Ref. 1 assumed the flowfield to be in thermochemical equilibrium. A comparison of results from the parametric study of Ref. 1 and those obtained in Ref. 3, however, suggested that for aerobrakes with small nose radii ($R_N^* < 2.3$ m) and altitudes greater than about 35 km, the flow may not be in chemical equilibrium. Since the aeroshell nose radius for the MESUR Pathfinder is 0.6625 m and the peak heating is predicted to occur at about 41-km altitude,
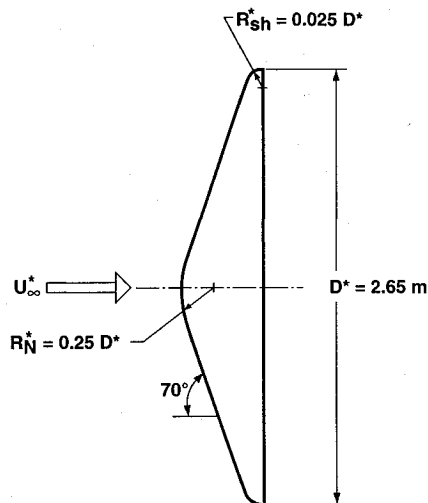
a chemical nonequilibrium calculation is required for designing the Pathfinder aerobrakes. Reference 4 recently showed that thermal nonequilibrium for the MESUR mission is negligible.

The purpose of this work is to discuss results from an aerothermodynamic study of the MESUR Pathfinder aeroshell shown in Fig. 1. The forebody of this Viking-type Pathfinder aerobrake is a 70-deg sphere cone with a nose radius of 0.6625 m, base diameter of 2.65 m, and shoulder radius of 0.06625 m. The atmospheric entry trajectory given in Table 1 (based on COSPAR summer mean model[5,6]) is considered for this analysis. Entry is defined to occur at an atltitude of 125.00 km, and the entry angle for the aerobrake with a ballistic coefficient ($m/C_D A$) of 55.00 kg/m^2 is -14.20 deg.

For present analysis, the VSL method of Ref. 7 has been modified to implement a 16-species (O, O$_2$, O$^+$, O$_2^+$, N, N$_2$, NO, NO$^+$, e$^-$, C, C$_2$, CO, CO$_2$, CN, C$^+$, and CO$^+$) reaction model for the Martian atmosphere. This model is adapted from the work of Ref. 8 and is consistent with the equilibrium chemistry model of Ref. 1. Since the concentrations of NO, NO$^+$, and O$_2^+$ are not significant under equilibrium conditions, these species were not included in Ref. 1. However, in a finite rate calculation, the molecular ions NO$^+$ and O$_2^+$ (and also CO$^+$), which attain a high concentration[8] immediately behind the shock wave, provide the initial free electrons needed for triggering the electron impact ionization processes. These processes in turn control the chemical equilibration process for the entire flowfield. Thus, the 16-species reaction model employed in this study is considered to be adequate and computationally efficient to analyze the thermochemical issues in the Martian atmosphere, consisting of a CO$_2$–N$_2$ mixture.

Since surface recombination model plays an important role in evaluating surface heating for a nonablating surface, a physically consistent model is proposed for the surface recombination of CO$_2$. An evaluation of this model is made by comparison with the equilibrium catalytic wall boundary condition. These finite rate surface heating results are compared with those obtained from the equilibrium chemistry calculations of Ref. 1, and an estimate is provided of chemical nonequilibrium through the trajectory given in Table 1. Results are obtained from a parametric study of the sensitivity of surface heating to the uncertainties in reaction rate constants, surface temperature, and the transport properties. Also, an evaluation of stagnation radiative heating is made through the trajectory for equilibrium chemistry. Finally, an evaluation of the reduction in heating with ablation (for equilibrium chemistry) is made at the trajectory peak-heating conditions.

Analysis

Flowfield Equations

The flow in the shock layer is assumed to be steady, laminar, and compressible over an axisymmetric body similar to that used for Martian and Earth entry studies.[1,9] The VSL equations employed[7,10] to analyze such a flow are those of a multicomponent reacting gas mixture in thermal equilibrium under conditions of chemical nonequilibrium and equilibrium. The present analysis provides a detailed description of the finite rate chemistry model, the surface recombination model for CO$_2$, and the flowfield thermodynamic and transport properties. The ablation injection and the radiative transport models (used with equilibrium chemistry) are those of Ref. 1.

Fig. 1   Aeroshell configuration for MESUR pathfinder.

Table 1   Freestream conditions for the Martian atmosphere ($C_{CO_2} = 0.97$ and $C_{N_2} = 0.03$) and stagnation-point heating for MESUR (Fig. 1)

Altitude, km	ρ_∞^*, kg/m^3	T_∞^*, K	p_∞^*, N/m^2	U_∞^*, km/s	$\bar{\varepsilon}_N$ or $Re_{\mathrm{ref},R_N^*}^{-\frac{1}{2}}$	M_∞	T_{REWT}^*,[a] K	$-q_w^*$, W/cm^2 Nonequilibrium NCW	$-q_w^*$, W/cm^2 Nonequilibrium FRCO$_2$	$-q_w^*$, W/cm^2 Equilibrium
74.28	0.497 × 10^{-5}	139	0.13	7.66	0.133	40.11	1663	20.17	37.32	35.19
59.97	0.359 × 10^{-4}	144	0.88	7.58	0.049	38.88	1987	21.00	72.63	71.89
47.27	0.153 × 10^{-3}	155	4.42	7.18	0.024	35.60	2247	32.07	118.90	111.97
40.70	0.323 × 10^{-3}	162	10.09	6.59	0.016	31.57	2288	41.42	126.63	120.87
36.87	0.501 × 10^{-3}	166	15.15	6.01	0.013	28.86	2239	36.25	112.09	111.60
29.43	0.105 × 10^{-2}	176	34.98	4.24	0.009	19.86	1835	14.47	33.40	51.76
24.54	0.171 × 10^{-2}	182	59.12	2.77	0.007	12.76	1349	13.80	14.77	15.07
21.23	0.236 × 10^{-2}	186	83.48	1.84	0.006	8.36	961	3.93	3.93	3.90

[a]The radiative-equilibrium wall temperature T_{REWT}^* used in all surface heating calculations is based on the equilibrium heating.

Gas-Phase Chemistry Model

For equilibrium as well as nonequilibrium flow, a 16-species (C, N, O, C_2, N_2, O_2, CN, CO, NO, CO_2, C^+, O^+, O_2^+, CO^+, NO^+, and e^-) chemistry model is employed for the shock-layer gas without surface ablation. For nonequilibrium flow, the species production terms $\dot{w}_i$ appearing in the energy and species continuity equations[7,10] are evaluated for 33 reactions[11] of the Martian atmosphere (97% CO_2 and 3% N_2). These reactions are taken primarily from Ref. 8 and have been supplemented by those provided in Refs. 12 and 13.

The forward reaction rate for the reactions is expressed in the modified Arrhenius form,[12] and the backward rate is obtained from the forward rate by employing the relation

$$k_{b,r}^* = k_{f,r}^*/K_{EQ,r} \tag{1}$$

where the equilibrium constant $K_{EQ,r}$ is curve-fitted[14] as

$$K_{EQ,r} = \exp\left(C_{1,r} + C_{2,r}\,\ell_n Z + C_{3,r}Z + C_{4,r}Z^2 + C_{5,r}Z^3\right) \tag{2a}$$

with

$$Z = 10{,}000/T^* \tag{2b}$$

The values of the various constants are tabulated in Tables 1 and 2 of Ref. 11. The corresponding third-body efficiencies relative to argon are given in Table 3 of the same reference.

Thermodynamic and Transport Properties

The equilibrium composition is determined by a free-energy minimization calculation.[15] Thermodynamic properties (specific heat, enthalpy, and free energy) and transport properties (viscosity and thermal conductivity) are required for each species considered. Values of these properties are obtained by using polynomial curve fits,[1,9] and the mixture viscosity is obtained by using a semiempirical formula.[16] A similar relation[16] is used to compute the mixture thermal conductivity. Both the Prandtl and Lewis numbers are employed, with either a constant or a variable value. Values of 0.62 and 1.0 are used for the calculations with constant Prandtl and Lewis number, respectively. Since CO and O are the main spcies in the outer parts of the shock layer and CO_2 and N_2 are the main species near the wall, the variable Lewis number is obtained from the following value of the effective diffusion coefficient for the mixture[16]:

$$\frac{1}{D_m^*} = \frac{1}{x_{CO_2} + x_{N_2} + x_{CO} + x_O}\left(\frac{x_{CO_2} + x_{N_2}}{D_{CO_2-N_2}^*} + \frac{x_{CO} + x_O}{D_{CO-O}^*}\right) \tag{3}$$

Radiative Transport

The radiation-transport code RADICAL[17,18] has been used with equilibrium chemistry to compute the radiative flux q_{rad} and its divergence Q. This code allows for the effects of nongray self-absorption and includes the molecular band, continuum, and atomic line transitions. As mentioned earlier, 16 chemical species (the same species as used in the nonequilibrium-flow chemistry model) are considered for computing the radiative transport in the Martian atmosphere in the absence of ablation. The ultraviolet properties for C_3 (for the case of surface ablation) are taken from Ref. 19.

Boundary Conditions

The boundary conditions at the shock are calculated by using the Rankine–Hugoniot relations. The flow behind the shock is assumed to be in chemical equilibrium or frozen at the freestream composition for equilibrium and nonequilibrium calculations, respectively.[10] No-slip continuum boundary conditions are employed at the surface. The wall temperature is either specified or calculated. For the calculated conditions, the surface temperature is assumed to be the radiative equilibrium wall value obtained from

$$T_{REWT}^* = \left[\bar{\varepsilon}_{sh}^2\left(K\frac{\partial T}{\partial n} + \frac{\mu Le}{Pr}\sum_{i=1}^{NS} h_i\frac{\partial C_i}{\partial n}\right)_w \frac{\rho_\infty^* U_\infty^{*3}}{\bar{\varepsilon}\sigma^*}\right]^{\frac{1}{4}} \tag{4}$$

where NS is the number of species. To make the surface-heating comparison with different flowfield chemistry, the surface temperature used with nonequilibrium chemistry calculations is the same

as that computed for equilibrium chemistry without radiation. The same value of the surface temperature is employed with radiation also.

Species boundary conditions for a nonablating surface are provided in the next subsection. For an ablating surface, values of the species concentrations, ablation rates, and surface temperatures have been computed from the charring material and ablation[20,21] (CMA) thermal response code by using the input surface heat flux obtained from a flowfield code, GIANTS.[22] SLA-561 was the heatshield material on the Viking Mars Landers built by the Martin Marietta Corporation.[23] For analyzing the case with surface ablation, O_2^+ is dropped and five more species (Si, SiO, C_3, H, and H_2) are included for a total of 20 species in the equilibrium chemistry model.

Catalytic Wall Boundary Condition

The rate at which reactions proceed at the surface is influenced by wall catalysis. The recombination reactions at a catalytic wall can occur through the following mechanism[24,25]: 1) diffusive transport of reactants to the surface, 2) adsorption of reactants on the surface, 3) chemical reactions between reactants adsorbed on the surface, 4) desorption of reactants and products from the surface, and 5) diffusive transport of reactants and products away from the surface.

For nonequilibrium flow, two extreme cases are analyzed for catalytic walls:

1) Noncatalytic wall (NCW): In this case no reactions can occur at the surface. Therefore, the mass-fraction gradient for all the species is zero at the surface, i.e.,

$$\left(\frac{\partial C_i}{\partial n^*}\right)_w = 0 \tag{5}$$

2) Equilibrium catalytic wall (ECW): The most practical way to implement this boundary condition is to assume that the wall-catalyzed reactions occur at an infinite rate so that the species mass fractions at the wall are those corresponding to their local equilibrium values:
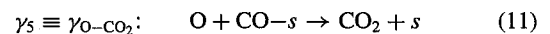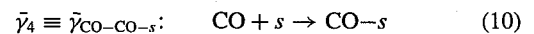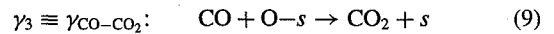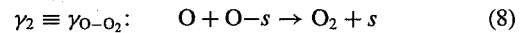
$$(C_i)_w = (C_i)_{EQ} \tag{6a}$$

where

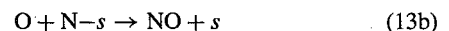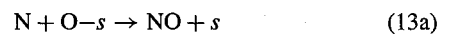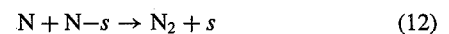$$(C_i)_{EQ} = f\left(p_w^*, T_w^*, \tilde{C}_{i,w}\right) \tag{6b}$$

If the surface temperature T_w^* is not too high, this condition will ensure that all gas species recombine completely to the freestream composition. The main deficiency of this boundary condition is that it does not allow for any diffusion limitation of reactants. A surface recombination model is developed next that does so. For equilibrium flow, Eqs. (6a) and (6b) are the appropriate boundary conditions and are not affected by diffusion limitation of the reactants.
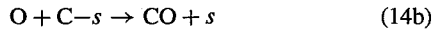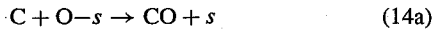
Wall Condition of Fully Recombined CO_2 (FRCO$_2$)

A full surface recombination model for CO_2 (limited by the diffusion of CO and O to the surface) is presented here. For this purpose, consider the following reactions at the surface, with their associated recombination and adsorption probabilities:

$$\bar{\gamma}_1 \equiv \bar{\gamma}_{O-O-s}: \qquad O + s \rightarrow O-s \tag{7}$$

$$\gamma_2 \equiv \gamma_{O-O_2}: \qquad O + O-s \rightarrow O_2 + s \tag{8}$$

$$\gamma_3 \equiv \gamma_{CO-CO_2}: \qquad CO + O-s \rightarrow CO_2 + s \tag{9}$$

$$\bar{\gamma}_4 \equiv \bar{\gamma}_{CO-CO-s}: \qquad CO + s \rightarrow CO-s \tag{10}$$

$$\gamma_5 \equiv \gamma_{O-CO_2}: \qquad O + CO-s \rightarrow CO_2 + s \tag{11}$$
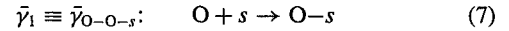
Since the concentrations of C and N near the surface are very small, the effect of the recombination reactions

$$N + N-s \rightarrow N_2 + s \tag{12}$$

$$N + O-s \rightarrow NO + s \tag{13a}$$

$$O + N-s \rightarrow NO + s \tag{13b}$$

$$C + O{-}s \rightarrow CO + s \qquad (14a)$$

$$O + C{-}s \rightarrow CO + s \qquad (14b)$$

on surface heating is negligible, and therefore, these are not included in the recombination model. In Eqs. (7–11), s is a surface site, and $\bar{\gamma}_i$ is an effective adsorption probability related to the adsorption rate coefficient $k^*_{ads,i}$, by the expression[24]

$$k^*_{ads,i} = \bar{\gamma}_i \sqrt{\frac{R^*_{univ} T^*_w}{2\pi M^*_i}} \qquad (15)$$

Similarly, the recombination probability γ_i of incident species i in Eqs. (7–11) is expressed in terms of the recombination rate coefficient k^*_i as[26]

$$k^*_i = \gamma_i \sqrt{\frac{R^*_{univ} T^*_w}{2\pi M^*_i}} \qquad (16)$$

Now, for maximum CO_2 recombination (i.e., $\gamma_2 = 0$), the two cases are:

1) There is abundant CO surface coverage, and the CO_2 recombination is limited only by the incident number flux of O. For this case

$$N^\downarrow_O < N^\downarrow_{CO} \qquad (17a)$$

where $N^\downarrow_O$ and $N^\downarrow_{CO}$ are the incident number fluxes of O and CO, respectively.

2) Incident O provides abundant surface coverage, and the CO_2 recombination is then limited by the incident number flux of CO:

$$N^\downarrow_{CO} < N^\downarrow_O \qquad (17b)$$

Case 1: $N^\downarrow_O < N^\downarrow_{CO}$

Since the net fluxes of CO and O are equal,

$$N^{net}_{CO} = N^{net}_O \qquad (18a)$$

or

$$(\gamma_3 + \bar{\gamma}_4)N^\downarrow_{CO} - N^{des}_{CO} = (\gamma_5 + \bar{\gamma}_1)N^\downarrow_O - N^{des}_O \qquad (18b)$$

Now, based on the Eley–Rideal mechanism[24,27,28] [where the surface recombination occurs between the adsorbed and gas phases species (recombination reactions governed by the Langmuir–Hinshelwood mechanism[24,27,28] that occur between the adsorbed species are not considered here)], the following values for the adsorption and recombination coefficients in Eq. (18b) are used to obtain the maximum possible CO_2 recombination:

$$\bar{\gamma}_1 = \gamma_3 = 0, \qquad \gamma_5 = 1$$
$$N^{des}_{CO} = N^{des}_O = 0 \qquad (19)$$

Since $N^\downarrow_O < N^\downarrow_{CO}$, every O that arrives at the surface reacts with the adsorbed CO (implying $\gamma_5 = 1$), and there is no O left for adsorption, meaning $\bar{\gamma}_1 = 0$. Further, since there is no adsorbed O, the reaction (9) cannot proceed ($\gamma_3 = 0$), and incident CO can only get adsorbed to the surface [the reaction (10)]. For maximum CO_2 recombination, it is desired that the desorption flux of CO (N^{des}_{CO}) be zero, and, in the absence of any adsorbed O, N^{des}_O will also be zero.

Thus, using Eq. (19) in Eq. (18b), one obtains

$$\bar{\gamma}_4 N^\downarrow_{CO} = N^\downarrow_O \qquad (20a)$$

and so, upon substitution for the incident number fluxes in terms of the particle number densities and their average velocities,[16,26] the following value for $\bar{\gamma}_4$ is obtained:

$$\bar{\gamma}_4 = \frac{C_{O,w}}{C_{CO,w}} \left(\frac{M^*_{CO}}{M^*_O}\right)^{\frac{3}{2}} \qquad (20b)$$

Case 2: $N^\downarrow_{CO} < N^\downarrow_O$

In the case with $N^\downarrow_{CO} < N^\downarrow_O$, every incident CO recombines with adsorbed O ($\gamma_3 = 1$), and there is no CO left for adsorption ($\bar{\gamma}_4 = 0$).

Since there is no adsorbed CO, the reaction (11) cannot proceed ($\gamma_5 = 0$). Further, to maximize CO_2 production, it is desired to have the desorbed flux of O (N^{des}_O) zero. In the absence of any adsorbed CO, N^{des}_{CO} will also be zero. Equation (18b) for this case becomes

$$N^\downarrow_{CO} = \bar{\gamma}_1 N^\downarrow_O \qquad (21a)$$

which, similarly to Eqs. (20), gives

$$\bar{\gamma}_1 = \frac{C_{CO,w}}{C_{O,w}} \left(\frac{M^*_O}{M^*_{CO}}\right)^{\frac{3}{2}} \qquad (21b)$$

Now, the surface boundary conditions for the various species can be written as follows:

1) For CO_2, the net mass flux is[26]

$$J^{*net}_{CO_2} = -J^{*net}_{CO} - J^{*net}_O \qquad (22a)$$

or

$$J^{*net}_{CO_2} = -\left[(\gamma_3 + \bar{\gamma}_4)J^{*\downarrow}_{CO} - J^{*des}_{CO}\right] - \left[(\gamma_5 + \bar{\gamma}_1)J^{*\downarrow}_O - J^{*des}_O\right] \qquad (22b)$$

with

$$J^{*net}_{CO_2} = -\rho^* D^*_m \frac{\partial C_{CO_2}}{\partial n^*}$$

$$\frac{J^{*\downarrow}_{CO}}{\rho^*} = -C_{CO} \sqrt{\frac{R^*_{univ} T^*_w}{2\pi M^*_{CO}}} \qquad (22c)$$

$$\frac{J^{*\downarrow}_O}{\rho^*} = -C_O \sqrt{\frac{R^*_{univ} T^*_w}{2\pi M^*_O}}$$

and for $N^\downarrow_O < N^\downarrow_{CO}$ [or $C_{O,w} < C_{CO,w}(M^*_O/M^*_{CO})^{3/2}$],

$$\bar{\gamma}_1 = \gamma_3 = 0$$

$$\bar{\gamma}_4 = \frac{C_{O,w}}{C_{CO,w}} \left(\frac{M^*_{CO}}{M^*_O}\right)^{\frac{3}{2}} \qquad (22d)$$

$$\bar{\gamma}_5 = 1$$

$$J^{*des}_{CO} = J^{*des}_O = 0$$

or for $N^\downarrow_O > N^\downarrow_{CO}$ [or $C_{O,w} > C_{CO,w}(M^*_O/M^*_{CO})^{3/2}$],

$$\bar{\gamma}_1 = \frac{C_{CO,w}}{C_{O,w}} \left(\frac{M^*_O}{M^*_{CO}}\right)^{\frac{3}{2}}$$

$$\bar{\gamma}_3 = 1 \qquad (22e)$$

$$\gamma_4 = \gamma_5 = 0$$

$$J^{*des}_{CO} = J^{*des}_O = 0$$

2) For CO, the net mass flux is

$$J^{*net}_{CO} = (\gamma_3 + \bar{\gamma}_4)J^{*\downarrow}_{CO} - J^{*des}_{CO} \qquad (23a)$$

where

$$J^{*net}_{CO} = -\rho^* D^*_m \left(\frac{\partial C_{CO}}{\partial n^*}\right)$$

$$\frac{J^{*\downarrow}_{CO}}{\rho^*} = -C_{CO} \sqrt{\frac{R^*_{univ} T^*_w}{2\pi M^*_{CO}}} \qquad (23b)$$

and γ_3, $\bar{\gamma}_4$, and J^{*des}_{CO} are given by Eqs. (22d) and (22e).

3) For O, the net mass flux is

$$J^{*net}_O = (\gamma_5 + \bar{\gamma}_1)J^{*\downarrow}_O - J^{*des}_O \qquad (24a)$$

where

$$J_0^{*net} = -\rho^* D_m^* \left(\frac{\partial C_O}{\partial n^*} \right)$$

$$\frac{J_0^{*\downarrow}}{\rho^*} = -C_O \sqrt{\frac{R_{univ}^* T_w^*}{2\pi M_O^*}}$$

(24b)

and $\bar{\gamma}_1$, γ_5, and J_0^{*des} are obtained from Eqs. (22d) and (22e).

4) For the rest of the species (i.e., $i \neq CO_2$, CO, and O) the surface boundary condition is obtained from

$$\frac{\partial C_i}{\partial n^*} = 0$$

(25)

Solution Procedure

The VSL solution method has been modified to analyze the Martian atmospheric flow past a 70-deg sphere–cone aeroshell with a shoulder as shown in Fig. 1. The sonic line lies close to the shoulder for such a wide-angle body. However, the flow becomes supersonic over the shoulder, which has a rather small radius ($R_{sh}^* = 0.1 R_N^*$). With a supersonic outflow boundary at the shoulder and the Vigneron pressure condition,[29] the VSL method has been globally iterated to obtain converged solutions. The numerical procedure used to solve the nonequilibrium and equilibrium VSL equations is a spatial-marching, implicit finite difference technique, which includes coupling of the global continuity and normal momentum equations and use of the Vigneron pressure condition[29] in the subsonic region (which covers a large part of the 70-deg sphere cone shown in Fig. 1).

To resolve the flowfield over the cone shoulder (see Fig. 1), it becomes necessary to use a much smaller stepsize than in the nose region. However, even with the small stepsize over the shoulder, the solution becomes unstable because of the large value of the curvature. This problem has been overcome by employing the shoulder radius R_{sh}^* for the reference length in place of the nose radius R_N^*, which is conventionally used. With this change, the nondimensional curvature over the shoulder, κ_{sh} ($= R_{sh}^*/R_{sh}^*$), and over the nose, κ_N ($= R_{sh}^*/R_N^*$), does not exceed one, and all quantities in the normalized equations[7,10] remain of the order of unity. This approach can be employed to analyze flowfields past bodies with very small shoulder radius compared to the nose radius. The change in reference length from R_N^* to R_{sh}^* results in an increase of the number of streamwise body stations, which can, however, be controlled by using a larger stepsize in the nose region than in the shoulder region. With the use of R_{sh}^*, the nondimensional form of the governing equations remains similar to that obtained[7,10] by employing R_N^*, except that the Reynolds-number parameter ε is now based on R_{sh}^* in place of R_N^*. However, this change in reference length changes the nondimensional form of the stagnation-line series solution which is employed to march the solution downstream. Therefore, a new series solution has been developed for the stagnation streamline by following the approach of Ref. 7. Beyond the stagnation line, the governing equations are solved as a parabolic set of equations using an implicit finite difference numerical procedure.[7] The VSL analysis provides a direct means of allowing for interactions between the inviscid and viscous flow regions because of entropy-layer swallowing, radiative transfer, and mass injection. The details of the method of solution are similar to those of Refs. 7 and 9 and therefore are not presented here.

Results and Discussion

Results are presented for the entry trajectory of the MESUR probe into the Martian atmosphere (see Fig. 1 and Table 1). The highest point analyzed in the trajectory is at an altitude of 74.28 km, where the Reynolds-number parameter $\bar{\varepsilon}_N$ has a value of about 0.13 (see Table 1). For values of $\bar{\varepsilon}_N$ less than about 0.15, assumptions of continuum flow and no slip are appropriate,[7] and therefore surface and shock slips are not included in the results obtained here. Calculations for the results are carried out on the Cray II computer at NASA Langley Research Center. A 100×105 grid is employed with all the computations. Variable grid sizes are used both normal to and along the body surface. The minimum distance between grid points normal to the body is $2 \times 10^{-4} R_{sh}^*$. In the direction along the surface, the minimum grid size is $1 \times 10^{-1} R_{sh}^*$ on the shoulder. The grid size employed in the nose region along the surface is as large as 5 times this value to reduce the computational time. These values of the grid sizes have been established to ensure grid independence of the solution for the cases analyzed here. The computational time required (measured in CPU seconds) is about 2000 and 3000 s per global pass for the calculations of nonequilibrium and equilibrium flow (without radiation) around the body, respectively. Typically, two global passes are required for convergence of the shock shape and surface heating.

Comparisons with Navier–Stokes (LAURA) Calculations of the Peak-Heating Point in the Trajectory

Before presenting results from detailed calculations, a comparison of the present VSL results is made with those obtained from the LAURA code.[30] Figure 2 compares the subsonic zones predicted by the two methods for the nonequilibrium flow. Since LAURA is a shock-capturing technique and the present VSL method employs a shock-fitting approach, Fig. 2 also shows the computational domain for LAURA and the shock location for VSL. The subsonic zones from the two calculations are predicted to be almost the same and extend right up to the shoulder, where the flow becomes supersonic. Figure 2, therefore, shows that the present VSL formulation (with cone-shoulder radius as the length scale) is capable of solving flows past wide-angle bodies with large subsonic regions.

Surface pressures and heat-transfer rates predicted by the VSL and LAURA methods are compared in Figs. 3a and 3b, respectively. The VSL predictions are for the nonequilibrium (with fully recombined CO_2 at the surface) and equilibrium flow conditions, whereas the LAURA predictions are for the nonequilibrium flow only. Pressures obtained by the two methods compare quite well, except for the shoulder, where the pressure has a sharper decrease for the VSL than for the LAURA calculations. Earlier studies[4,3] with LAURA also showed a sharper decrease in pressure over the shoulder (similar to the present and earlier[31] VSL predictions). As compared to the pressure, there is a bigger difference in the surface heat transfer rates predicted by the two methods. The nonequilibrium VSL stagnation heating rate (with fully recombined CO_2) is about 11% greater than the corresponding LAURA value. The equilibrium VSL heating rate is similar to the nonequilibrium VSL prediction with a difference of about 4.5% at the stagnation point. A value of the surface heat transfer rate is also computed from the cold-wall equilibrium correlation because of Sutton and Graves,[32] which for 97% CO_2 and 3% N_2 is

$$q_w^* = 18.9 U_\infty^{*3} \sqrt{\rho_\infty^*/R_N^*}$$

(26)

where q_w^* is in W/cm^2 and U_∞^* is in km/s. This correlation (based on boundary-layer calculations) gives a stagnation-point value of 119.54 W/cm^2, which is within about 1% of the equilibrium VSL value.

The difference in surface heating values predicted by the VSL and LAURA methods is primarily because of the differences in the
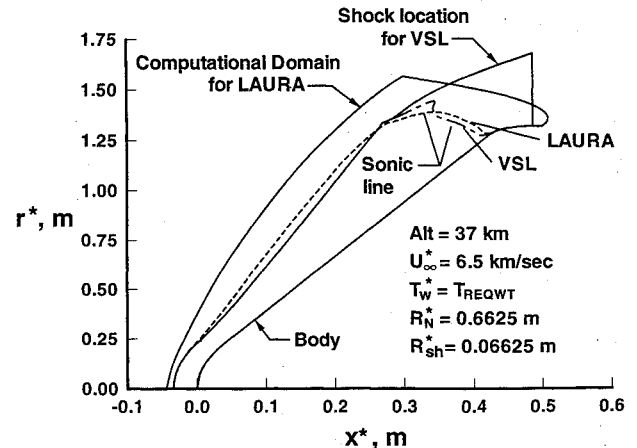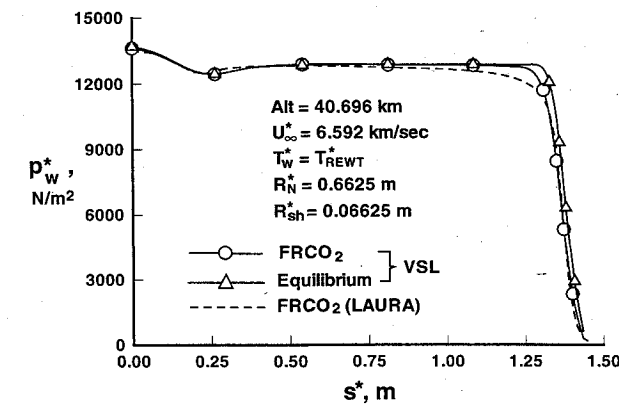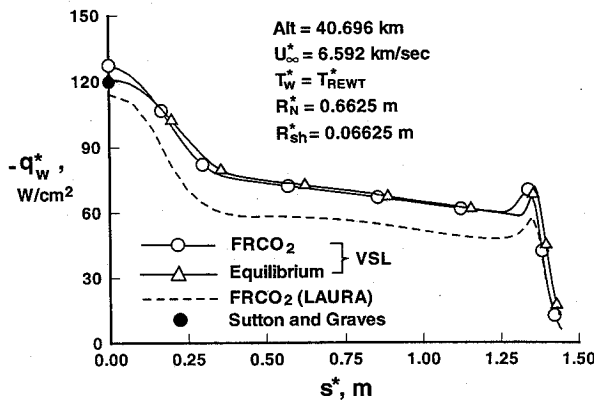
Fig. 2 Comparison of subsonic zone predictions by VSL and LAURA calculations.

a) Pressure

b) Heat transfer rate

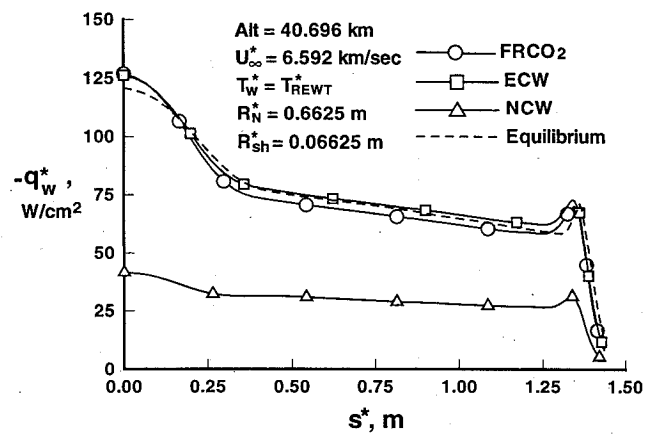Fig. 3 Comparison of surface quantities predicted by VSL and LAURA calculations.

a) Surface heat transfer rate

b) Radiative-equilibrium wall temperature

c) Surface distribution of CO_2 mass fraction

Fig. 4 Effect of variation in surface recombination model.

diffusion coefficients employed in the two calculations. The effective D_m^* from Eq. (3) gives a value similar to that for the CO_2–N_2 pair at surface for a fully recombined CO_2 case. The diffusion mass fluxes using D_m^* from Eq. (3) sum to zero, as required by the conservation of fluxes. LAURA employs a more general method for obtaining the diffusion coefficients [see Eq. (29) in the next subsection]. However, the diffusion mass fluxes using these values of the diffusion coefficients do not necessarily sum to zero in LAURA calculations. Therefore, even with similar mass-fraction profiles obtained from the VSL and LAURA calculations, a slight elemental separation is seen [see Fig. 5b of Ref. 11] in LAURA predictions. This elemental separation results in different values of the diffusion coefficient, which in turn give different surface heating rates.[33] Other factors such as grid singularity and grid resolution, which affect LAURA heating predictions, are discussed in Ref. 31.

Sensitivity Studies Affecting Surface Heating

Since the accuracy of numerical calculations can only be evaluated through an evaluation of the physicochemical models employed, it is desirable to evaluate the sensitivity of surface heating (and other flowfield quantities) to variations in values of the parameters employed in these models. Without such an evaluation, an assessment of the accuracy of surface heating obtained from a numerical calculation is meaningless. For this purpose, the peak-heating point in the trajectory (altitude 40.70 km) is chosen, and a parametric study is performed to evaluate the effect of variations in the surface catalysis model, gas-phase reaction rate coefficient, surface temperature, and transport properties.

Effect of Variation in Surface Catalysis Model

Figure 4a shows the effect of different surface recombination (or catalysis) models on surface heating. As mentioned in the boundary-conditions section, the three recombination boundary conditions employed with the nonequilibrium predictions are NCW, ECW, and
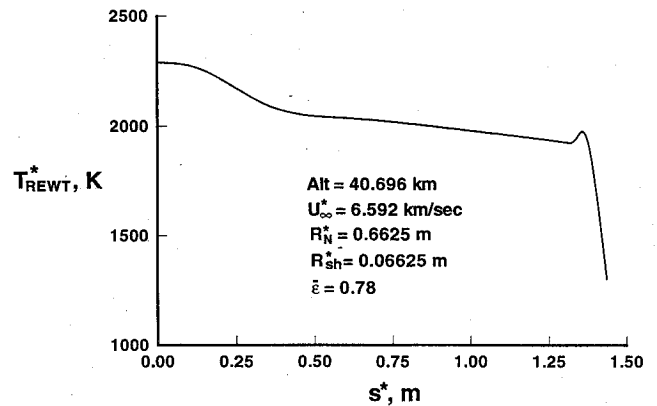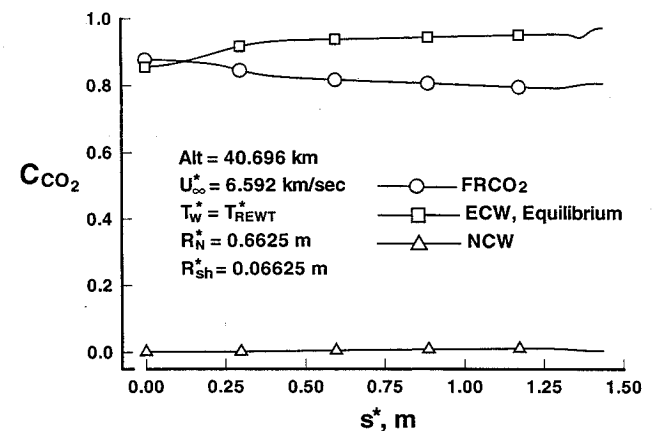
fully recombined CO_2 (FRCO_2). Also shown for comparison is the prediction obtained from a fully equilibrium calculation. The radiative equilibrium wall temperature (T_{REWT}^*) employed with the calculations is that obtained from a fully equilibrium calculation and is given in Fig. 4b. The surface distribution of CO_2, shown in Fig. 4c, indicates a smaller recombined value for CO_2 (except at the stagnation point) than for the ECW calculations, because of the diffusion limitation of CO and O reaching the surface. At the stagnation point, the FRCO_2 value is higher than the ECW value because of the full CO_2 recombination employed there, even though the surface temperature may be high enough to dissociate CO_2 (as suggested by the ECW calculation). It is suggested that the presently obtained FRCO_2 boundary condition may be more appropriate than the ECW boundary condition for the nonequilibrium calculations when the diffusion limitation of the reactants exists and the surface temperatures allow for CO_2 to stay fully recombined. The surface
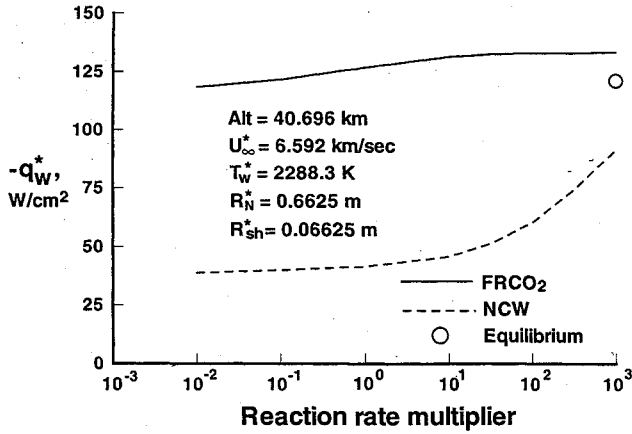
Fig. 5 Effect of uncertainty in dissociation rate of CO_2 on stagnation-point heating.
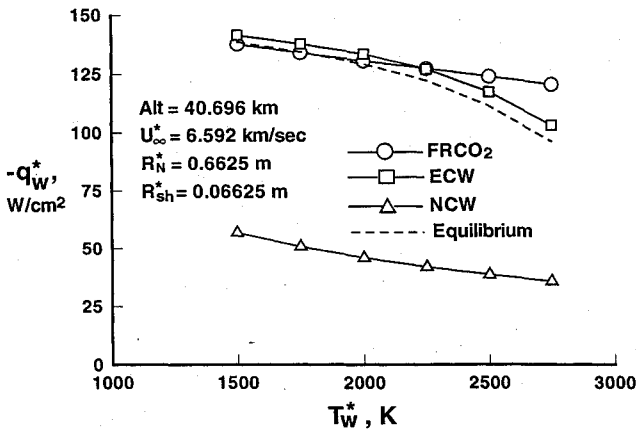

Fig. 6 Effect of uncertainty in surface temperature on stagnation-point heating.

heating distributions of Fig. 4a are consistent with the CO_2 surface distributions. Higher values of the recombined CO_2 result in larger surface heating. The nonequilibrium NCW value at the stagnation point is about one-third of the $FRCO_2$ value. The small difference between the nonequilibrium ECW and the fully equilibrium surface-heating calculation is because of the differences in the flow-field chemistry.

Effect of Uncertainty in Gas-Phase Reaction Rate

Since the dissociation of CO_2 is the primary reaction in the shock layer, an evaluation of the effect of uncertainty in the dissociation rate on surface heating is made by multiplying the dissociation and recombination rates by factors of 10 in the range of 10^{-2}–10^3. Figure 5 shows the stagnation-point heating for $FRCO_2$ and NCW surface boundary conditions. With a larger value of the reaction-rate multiplier, the flowfield chemistry tends towards equilibrium, and in that limit the difference between the $FRCO_2$ and NCW values should disappear. Also shown for comparison is a result from fully equilibrium calculation. Clearly, the heating predictions obtained with the NCW boundary condition are more sensitive to larger values of the reaction rates than in the $FRCO_2$ calculations.

Effect of Uncertainty in Surface Temperature

Because of uncertainties in the surface emissivity, the surface heating rate, the radiative cooling from the surface, and its heat-sink capability, it is difficult to specify the radiative-equilibrium wall temperature exactly. Figure 6 shows the effect of this uncertainty on stagnation-point heating. The dependence of nonequilibrium NCW and $FRCO_2$ calculations on the surface temperature appears to be similar. Predictions from ECW and fully equilibrium calculations seem to be more influenced by a temperature increase, especially at higher surface temperatures.
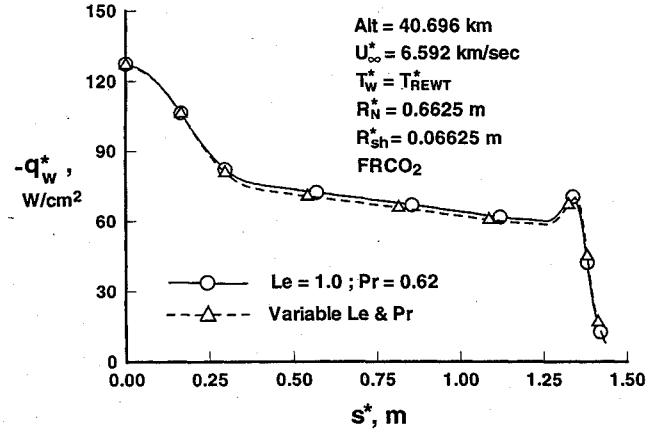

Fig. 7 Effect of variable Lewis and Prandtl numbers on surface heating distribution.

Effect of Variation in Lewis- and Prandtl-Number Values (Sensitivity to Transport Properties)

The mass flux of species i is obtained from Fick's law of diffusion:

$$J_i^* = -\rho^* D_m^* \frac{\partial C_i}{\partial n^*} = -\frac{Le}{Pr} \mu^* \frac{\partial C_i}{\partial n^*} \qquad (27)$$

where the Lewis and Prandtl numbers are defined, respectively, as

$$Le = \frac{\rho^* D_m^* C_{pf}^*}{K^*} \qquad Pr = \frac{C_{pf}^* \mu^*}{K^*} \qquad (28)$$

and the effective diffusion coefficient for the mixture, D_m^*, is given by Eq. (3). Similar to Eq. (3), an effective diffusion coefficient is also obtained from LAURA calculations[30]:

$$\frac{1}{D_m^*} = \sum_{i=1}^{NS} \frac{x_i}{D_{im}^*} \qquad (29a)$$

where D_{im}^* is defined as[16]

$$D_{im}^* = \frac{1 - x_i}{\sum_{j=1, j \neq i}^{NS} x_j / D_{i-j}^*} \qquad (29b)$$

and D_{i-j}^* is the binary diffusion coefficient for species pair $i - j$.

Since CO and O are the dominant species through much of the shock layer and CO_2 and N_2 are the dominant species at the shock (in the VSL shock-fitting formulation for nonequilibrium flow) and near the surface, the physics contained in Eq. (3) gives D_m^* comparable to that obtained from a more detailed calculation using Eq. (29). The Lewis-number value based on D_m^* changes appropriately[11] from that based on $D_{CO_2-N_2}^*$ at the surface to that based on D_{CO-O}^* through the shock layer and again to that based on $D_{CO_2-N_2}^*$ at the shock. The surface value of the Lewis number based on D_m^* and $D_{CO_2-N_2}^*$ is about 1.0, and the Prandtl number is about 0.62. A comparison of the surface heat transfer using these constant values for Le and Pr numbers as well as their variable values [with D_m^* obtained from Eq. (3)] is given in Fig. 7; no appreciable difference is observed in the two results. Thus, these constant values of Pr and Le may be used to obtain surface heating with a fair degree of accuracy.

Calculations Along the Trajectory

Figures 8 and 9 show results from the stagnation-point calculation carried out along the trajectory for the various altitude locations. Some of these results are also provided in Table 1. The nonequilibrium $FRCO_2$ convective results (Fig. 8) are similar to those obtained from a fully equilibrium calculation, except for the altitude of 29.43 km. There is a smaller amount of CO_2 recombination from the $FRCO_2$ calculation at this altitude than from the equilibrium result (see Fig. 4c). This is the result of diffusion limitation on CO and O reaching the surface to form CO_2 as mentioned earlier. The lowest heating is obtained for NCW, where the CO_2
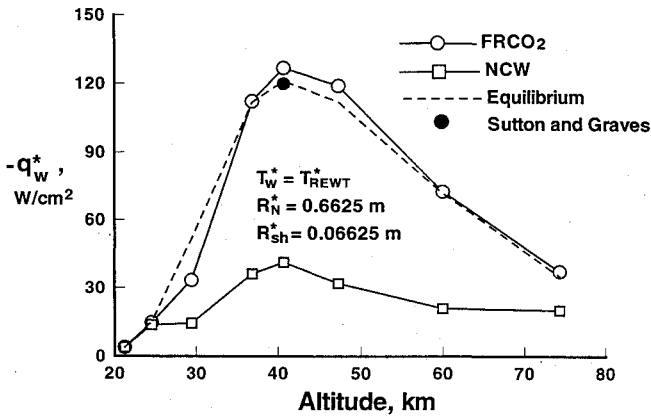
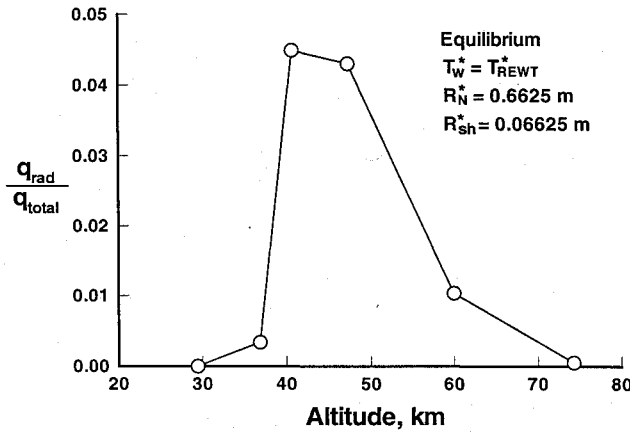Fig. 8   Stagnation-point convective heating along the trajectory.

Fig. 9   Stagnation-point radiative heating ratio along the trjectory.

recombination is smallest, as expected. Also shown for comparison is a calculation from the cold-wall equilibrium correlation[32] of Ref. 30 at the peak-heating altitude of 40.70 km. This result compares well with the equilibrium calculations. Flow in the shock layer approaches equilibrium at lower altitudes, and the effect of the surface boundary condition disappears from the surface heating. The radiative-equilibrium wall temperature obtained from the fully equilibrium calculations is employed with the calculations of Figs. 8 and 9. Figure 9 gives an estimate of equilibrium radiative heating[1] as a fraction of the total (convective + radiative) heating. A maximum value of 4.5% of the total heating is observed for the equilibrium radiative component at the peak-heating altitude of 40.70 km. Thus, it is negligible for most of the trajectory. No calculations were done for nonequilibrium radiative heating.

Calculation with Ablation at the Peak-Heating Altitude (40.70 km)

Some results have been obtained from the equilibrium chemistry calculations with and without ablation at the peak-heating altitude of 40.70 km. As mentioned earlier, the boundary conditions for an ablating surface [namely, T^*_{ABL}, $\dot{m}^*$, and (C_{i-}) (species concentrations of ablation species)] have been obtained at the NASA Ames Research Center from the one-dimensional CMA transient thermal response code[20,21] by employing the input surface heat flux obtained from a flowfield code, GIANTS.[22] The ablation boundary conditions are shown in Fig. 10. It should be mentioned here that the elemental composition obtained from the CMA-predicted species mass fractions is used to obtain the equilibrium mass fractions, $(C_i)_-$, of ablation species.[11] The surface species mass fractions $(C_i)_w$ are related to ablation species mass fractions $(C_i)_-$ by

$$\left(-J^*_i \right)_w = \dot{m}^*_w [(C_i)_w - (C_i)_-]   \tag{30a}$$

where $\dot{m}^*_w$ is the mass-injection rate of ablation species:

$$\dot{m}^*_w = (\rho^* v^*)_-   \tag{30b}$$
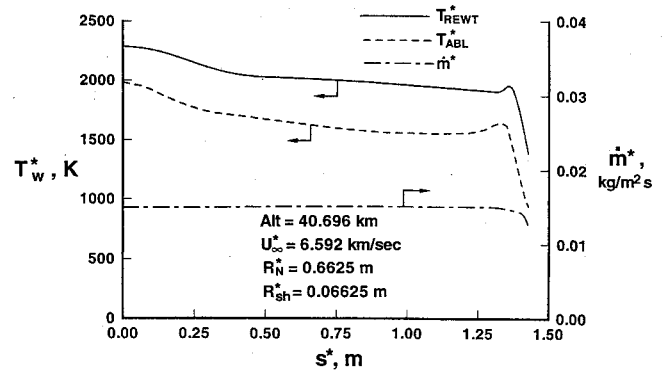

Fig. 10   Surface boundary conditions employed with ablation.
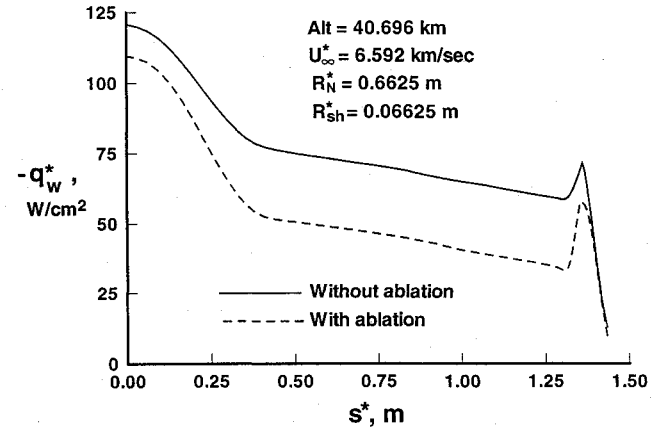

Fig. 11   Surface heating distribution with and without ablation.

For ablation injection, the elemental concentrations at the wall are governed by convection and diffusion [similarly to Eq. (30a)] and are obtained from

$$\left(\frac{\partial \tilde{C}_k}{\partial n} \right)_w - \frac{\dot{m}_w}{\bar{\varepsilon}^2_{sh}} \left(\frac{Pr}{\mu Le} \right)_w [(\tilde{C}_k)_w - (\tilde{C}_k)_-] = 0   \tag{31}$$

and the heat transferred to the wall by conduction, diffusion, and ablation is

$$-q_w = \bar{\varepsilon}^2_{sh} \left[\left(K \frac{\partial T}{\partial n} + \mu \frac{Le}{Pr} \sum_{i=1}^{NS} h_i \frac{\partial C_i}{\partial n} \right)_w \right.$$

$$\left. - \dot{m}_w \sum_{i=1}^{NS} [(C_i h_i)_w - (C_i h_i)_-] \right]   \tag{32}$$

The surface heating without ablation (Fig. 11) is obtained by using T^*_{REWT} given in Fig. 10. There is a reduction of about 9% in the stagnation heating because of ablation. The reduction is much larger (as much as 44%) on the conical flank. It should be mentioned here that the ablation rate $\dot{m}^*$ is small, which implies that both the shock-layer and ablation species are present at the surface. Because of the small ablation injection rate, shock-layer penetration by the ablation species is also small[11] (limited to $\bar{\eta} < 0.20$). Further, elemental separation because of ablation is not found in the absence of ablation, as seen from the constant values of the elemental mass fractions of C, N, and O through the shock layer.[11]

Conclusions

An aerothermodynamic study of the Mars Pathfinder aeroshell has been carried out through a VSL analysis with and without surface ablation. Results presented here are among the earliest VSL calculations for a wide-angle body with a shoulder.

The aeroshell consists of a 70-deg sphere cone with a shoulder radius one-tenth that of the nose. For proper resolution of the flowfield at the shoulder, the VSL equations are scaled with the shoulder radius in place of the conventionally employed nose radius. These

equations are globally iterated with the Vigneron pressure condition to treat the large embedded subsonic region between the stagnation line and the supersonic outflow at top of the shoulder. Good agreement on the extent of the subsonic region and the surface pressure is obtained with the Navier–Stokes calculations of the LAURA code.

The nonequilibrium VSL calculations (without ablation) employ a 16-species reaction model for the Martian atmosphere. Also, a physically consistent model is implemented for the surface recombination of CO_2. This recombination model allows for the diffusion limitation of CO and O in reaching the surface. Computed surface heating results with this model are consistent with those obtained from an ECW boundary condition when diffusion limitation of the reactants is not important. For both the ECW boundary condition (used with the nonequilibrium calculations) and the fully equilibrium computations, the same 16 species are used with a free-energy minimization procedure.

A parametric study of various factors affecting the surface heating was carried out at the peak heating altitude of the Martian trajectory analyzed. The surface catalysis model plays the most important role in heating prediction, as expected. A heating reduction of almost two-thirds is obtained for a NCW as compared to a surface with full CO_2 recombination. Uncertainties in gas-phase reaction rates and surface temperature affect surface heating much less. Values of 1.0 and 0.62 for the Lewis and Prandtl numbers, respectively, result in surface heating predictions almost the same as those obtained with their variable values.

The maximum stagnation heating of about 127 W/cm^2 is obtained with nonequilibrium calculations for the fully recombined CO_2 case at the peak heating point in Martian trajectory. Equilibrium calculations give almost the same value. A comparison between the nonequilibrium calculations with the NCW and equilibrium stagnation-point predictions along the trajectory shows the flow to be essentially in equilibrium for altitudes less than about 25 km. An estimate of the radiative heating (obtained from the equilibrium calculations) shows it to be negligible (<4.5% of the total heating) for the entire trajectory.

Calculations have also been carried out to evaluate the reduction in heating because of ablation. A decrease of about 9% in the stagnation-point heating (with equilibrium chemistry) is obtained at the peak-heating point in the trajectory.

Acknowledgments

References

[1]Gupta, R. N., Lee, K. P., Moss, J. N., and Sutton, K., "Viscous Shock-Layer Analysis of the Martian Aerothermal Environment," *Journal of Spacecraft and Rockets*, Vol. 29, No. 5, 1992, pp. 633–640.

[2]Hubbard, G. S., Wercinski, P. F., Sarver, G. L., Hanel, R. P., and Ramos, R., "A Mars Environmental Survey (MESUR)—Feasibility of a Low Cost Global Approach," International Astronautical Federation, Paper 91-432, Oct. 1991.

[3]Candler, G. V., "Computation of Thermo-Chemical Nonequilibrium Martian Atmosphere Entry Flows," AIAA Paper 90-1695, Jan. 1990.

[4]Mitcheltree, R., "Aerothermodynamics of a MESUR Martian Entry," AIAA Paper 93-2761, July 1993.

[5]Seiff, A., and Kirk, D. B., "Structure of the Atmosphere of Mars in Summer at Mid-Latitudes," *Journal of Geophysical Research*, Vol. 82, Sept. 1977, pp. 4364–4378.

[6]Pitts, D. E., Tillman, J. E., Johnson, N. C., Murphy, J., Pollack, J., Colburn, D. S., Haberle, R. M., Zurek, R., and Stewart, I., "The Mars Atmosphere—Observations and Model Profiles for Mars Mission," NASA Johnson Space Flight Center, JSC-24455, Dec. 1991.

[7]Lee, K. P., and Gupta, R. N., "Viscous Shock-Layer Analysis of Hypersonic Flows over Long Slender Vehicles," NASA CR-189614, March 1992.

[8]Park, C., Howe, J. T., Jaffe, R. L., and Candler, G. V., "Review of Chemical Kinetic Problems of Future NASA Mission, II: Mars Entries," *Journal of Thermophysics and Heat Transfer*, Vol. 8, No. 1, 1994, pp. 9–23.

[9]Gupta, R. N., Lee, K. P., Moss, J. N., and Sutton, K., "Viscous Shock Layer Solutions with Coupled Radiation and Ablation for Earth Entry," *Journal of Spacecraft and Rockets*, Vol. 29, No. 2, 1992, pp. 173–181.

[10]Gupta, R. N., Lee, K. P., and Zoby, E. V., "Enhancements to Viscous Shock-Layer Technique," *Journal of Spacecraft and Rockets*, Vol. 30, No. 4, 1993, pp. 404–413.

[11]Gupta, R. N., and Lee, K. P., "An Aerothermal Study of MESUR Pathfinder Aeroshell," AIAA Paper 94-2025, June 1994.

[12]McKenzie, R. L., "An Estimate of the Chemical Kinetics Behind Normal Shock Waves in Mixtures of Carbon Dioxide and Nitrogen for Conditions Typical of Mars Entry," NASA TN D-3287, Feb. 1966.

[13]Evans, J. S., Schexnayder, C. J., Jr., and Grose, W. L., "Effects of Nonequilibrium Ablation Chemistry on Viking Radio Blackout," *Journal of Spacecraft and Rockets*, Vol. 11, No. 2, 1974, pp. 84–88.

[14]Candler, G. V., private communication, Univ. of Minnesota, Minneapolis, MN, Dec. 1992.

[15]Stroud, C. W., and Brinkley, K. L., "Chemical Equilibrium of Ablation Materials Including Condensed Species," NASA TN D-5391, 1969.

[16]Bird, R. B., Stewart, W. E., and Lightfoot, E. N., *Transport Phenomena*, Wiley, New York, 1960, pp. 20, 24, 258.

[17]Nicolet, W. E., "Advanced Methods for Calculating Radiation Transport in Ablation Product Contaminated Boundary Layers," NASA CR-1656, Sept. 1970.

[18]Nicolet, W. E., "User's Manual for the Generalized Radiation Transfer Code (RAD/EQUIL)," NASA CR-116353, Oct. 1969.

[19]Shinn, J. L., "Optical Absorption of Carbon and Hydrogen Species from Shock Heated Acetylene and Methane in the 135–220 m Wavelength Range," *Thermophysics of Atmospheric Entry*, edited by T. E. Horton, Vol. 82, Progress in Astronautics and Aeronautics, AIAA, New York, 1982, pp. 68–80.

[20]Bartett, E. P., and Kendall, R. M., "An Analysis of the Coupled Chemically Reacting Boundary Layer and Charring Ablator," Pt. 3, NASA CR-1062, June 1968.

[21]Anon., "Aerotherm Charring Material Thermal Response and Ablation Program (CMA 87S)," Acurex, Rept. UM-87-13/ATD, Mountain View, CA, Nov. 1987.

[22]Chen, Y.-K., and Henline, W. D., "Analysis of Hypersonic Arcjet Flow Fields and Surface Heating of Blunt Bodies," AIAA Paper 93-0272, Jan. 1993.

[23]Anon., "Entry Data Analysis for Viking Landers," NASA CR-159388, 1976.

[24]Warnatz, J., "Resolution of Gas Phase and Surface Combustion into Elementary Reactions," *Twenty-Fourth Symposium (International) on Combustion*, Combustion Inst., Pittsburgh, PA, 1992, pp. 553–579.

[25]Taylor, H. S., "Combustion Processes," *High Speed Aerodynamics and Jet Propulsion Series*, edited by B. Lewis, Vol. 2, Princeton Univ. Press, Princeton, NJ, 1956.

[26]Gupta, R. N., Scott, C. D., and Moss, J. N., "Slip Boundary Equations for Multicomponent Nonequilibrium Airflow," NASA TP-2452, Nov. 1985, p. 10.

[27]Seward, W. A., and Jumper, E. J., "Model for Oxygen Recombination on Silicon Dioxide Surfaces," *Journal of Thermophysics and Heat Transfer*, Vol. 5, No. 3, 1991, pp. 284–291.

[28]Willey, R. J., "Comparison of Kinetic Models for Atom Recombination on High-Temperature Reusable Surface Insulation," *Journal of Thermophysics and Heat Transfer*, Vol. 7, No. 1, 1993, pp. 55–62.

[29]Gupta, R. N., Lee, K. P., Zoby, E. V., Moss, J. N., and Thompson, R. A., "Hypersonic Viscous Shock-Layer Solutions over Long Slender Bodies—Part 1: High Reynolds Number Flows," *Journal of Spacecraft and Rockets*, Vol. 27, No. 2, 1990, pp. 175–184.

[30]Mitcheltree, R. A., and Gnoffo, P. A., "Wake Flow About a MESUR Mars Entry Vehicle," AIAA Paper 94-1958, June 1994.

[31]Greene, F. A., and Gupta, R. N., "Viscous Equilibrium Computations Using Program LAURA," *Journal of Spacecraft and Rockets*, Vol. 29, No. 5, 1992, pp. 627–632.

[32]Sutton, K., and Graves, R. A., "A General Stagnation-Point Convective Heating Equation for Arbitrary Gas Mixtures," NASA TR R-376, Nov. 1971.

[33]Zoby, E. V., Gupta, R. N., and Lee, K. P., "Hypervelocity Stagnation-Point Heating Rate Discrepancies," *Journal of Spacecraft and Rockets*, Vol. 30, No. 6, 1993, pp. 773, 774.

T. C. Lin
Associate Editor